

Article

Enhanced Sulfate Formation from Gas-Phase SO₂ Oxidation in Non-•OH-Radical Environments

Xiaofan Lv¹, Makroni Lily¹, Stanley Numbonui Tasheh² , Julius Numbonui Ghogomu^{2,3}, Lin Du^{1,*} 
and Narcisse Tsona Tchinda^{1,*}

¹ Environment Research Institute, Shandong University, Qingdao 266237, China; xiaofanlv@mail.sdu.edu.cn (X.L.); makronilily@sdu.edu.cn (M.L.)

² Department of Chemistry, Faculty of Science, The University of Bamenda, Bamenda P.O. Box 39, Cameroon; tashestanley@uniba.cm (S.N.T.); ghogomujulius@uniba.cm (J.N.G.)

³ Research Unit of Noxious Chemistry and Environmental Engineering, Department of Chemistry, Faculty of Science, University of Dschang, Dschang P.O. Box 67, Cameroon

* Correspondence: lindu@sdu.edu.cn (L.D.); tsonatch@sdu.edu.cn (N.T.T.)

Abstract: Recent research on atmospheric particle formation has shown substantial discrepancies between observed and modeled atmospheric sulfate levels. This is because models mostly consider sulfate originating from SO₂ oxidation by •OH radicals in mechanisms catalyzed by solar radiation while ignoring other pathways of non-radical SO₂ oxidation that would substantially alter atmospheric sulfate levels. Herein, we use high-level quantum chemical calculations based on density functional theory and coupled cluster theory to show that monoethanolamine (MEA), a typical alkanolamine pollutant released from CO₂ capture technology, can facilitate the conversion of atmospheric SO₂ to sulfate in a non-•OH-radical oxidation mechanism. The initial process is the MEA-induced SO₂ hydrolysis leading to the formation of HOSO₂⁻•MEA⁺. The latter entity is thereafter oxidized by ozone (O₃) and nitrogen dioxide (NO₂) to form HSO₄⁻•MEA⁺, which is an identified stabilizing entity in sulfate-based aerosol formation. Results show that the HOSO₂⁻•MEA⁺ reaction with O₃ is kinetically and thermodynamically more feasible than the reaction with NO₂. The presence of an additional water molecule further promotes the HOSO₂⁻•MEA⁺ reaction with O₃, which occurs in a barrierless process, while it instead favors HONO formation in the reaction with NO₂. The investigated pathway highlights the potential role alkanolamines may play in SO₂ oxidation to sulfate, especially under conditions that are not favorable for •OH production, thereby providing an alternative sulfate source for aerosol modeling. The studied mechanism is not only relevant to sulfate formation and may effectively compete with reactions with sulfur dioxide and hydroxyl radicals under heavily polluted and highly humid conditions such as haze events, but also an important pathway in MEA removal processes.

Keywords: SO₂ oxidation; amine; sulfate; atmospheric fate; aerosol



Citation: Lv, X.; Lily, M.; Tasheh, S.N.; Ghogomu, J.N.; Du, L.; Tsona Tchinda, N. Enhanced Sulfate Formation from Gas-Phase SO₂ Oxidation in Non-•OH-Radical Environments. *Atmosphere* **2024**, *15*, 64. <https://doi.org/10.3390/atmos15010064>

Academic Editors: Shan Huang and Wei Wei Hu

Received: 25 November 2023

Revised: 19 December 2023

Accepted: 29 December 2023

Published: 3 January 2024



Copyright: © 2024 by the authors. Licensee MDPI, Basel, Switzerland. This article is an open access article distributed under the terms and conditions of the Creative Commons Attribution (CC BY) license (<https://creativecommons.org/licenses/by/4.0/>).

1. Introduction

Secondary atmospheric aerosol particles, formed from gas-to-particle conversion, are primarily composed of sulfate, which is one of the major water-soluble inorganic species in the atmosphere [1,2]. These particles are of great concern for their ability to affect human health, reduce visibility, acidify rainwater, and to alter the radiation balance of the atmosphere [3–5]. The main source of atmospheric sulfate is from the photooxidation of sulfur dioxide (SO₂) [6] and although a large number of studies have connected the formation rate of secondary atmospheric aerosol particles to atmospheric sulfate concentration [7–10], numerical models still fail to reproduce observed atmospheric sulfate concentrations [11]. This has led to considerable debate regarding the mechanisms responsible for sulfate formation, especially during winter haze events where sunlight radiation is weakened [3,12,13]. The incomplete understanding of the sulfate formation mechanism substantially hinders

the efficient prediction of haze events, climate change, air quality monitoring, and the development and implementation of measures to mitigate air pollution [14].

Recently, numerous researchers have focused on atmospheric sulfate formation mechanisms and, most importantly, on how they alter aerosol formation rates under severe pollution conditions. Sulfate is formed from the oxidation of sulfur dioxide (SO_2), primarily by hydroxyl radicals ($\bullet\text{OH}$) in the gas phase and ozone (O_3), nitrogen oxides (NO_x), hydrogen peroxide (H_2O_2), and O_2^- catalyzed by transition metal ions in aqueous-phase and cloud droplets [15–17]. Multiphase oxidation of SO_2 on solid or aqueous particles is considered a potentially important source of sulfate in the atmosphere as well [18]. Although various SO_2 oxidation pathways have been identified, the sources of sulfate and the relative importance of the various SO_2 oxidation pathways for sulfate formation in the atmosphere are yet to be clarified. For example, significant increases in sulfate concentrations were observed during haze events, but their sources remain elusive [19].

The primary gas-phase oxidant, $\bullet\text{OH}$ radical, is produced from excited oxygen and water under solar ultraviolet radiation. Despite the fast oxidation of SO_2 by $\bullet\text{OH}$ that initially forms sulfur trioxide (SO_3), which is further hydrolyzed to form sulfate, many observations have indicated that there is insufficient $\bullet\text{OH}$ in the atmosphere to account for the generally observed increasing sulfate formation in polluted environments [12,20]. Such low solar ultraviolet radiation conditions are particularly pronounced during haze events. Although the abundance of other oxidants (O_3 , H_2O_2 , NO_x) is relatively high, their reactions with SO_2 are generally hindered by high energy barriers. This suggests that important alternative pathways for atmospheric sulfate formation do exist, yet they have not been extensively investigated.

Atmospheric bases, including ammonia and amines, are other important components of secondary aerosols. Besides alkylamines such as methylamine and dimethylamine that have been identified as key species in sulfate aerosol formation [21], monoethanolamine (MEA, $\text{H}_2\text{NCH}_2\text{CH}_2\text{OH}$), a typical alkanolamine, has been found to enhance new particle formation as well and to stabilize acidic particles [22,23]. MEA is the most widely used baseline solvent in amine-based post-combustion CO_2 capture (PCC) technology [24,25]. Considering the potential large-scale implementation of amine-based PCC, relatively large amounts of MEA and possibly other alkanolamines may be emitted into the atmosphere from PCC units due to their relatively high vapor pressure [26,27]. It is estimated that nearly 80 tons of MEA may be released into the atmosphere from a CO_2 capture unit that removes 1 million tons of CO_2 per year [21,28] thereby increasing the environmental risk that MEA may potentially pose. Many studies have shown that atmospheric SO_2 conversion can be facilitated by the degradation of amines despite the lack of proper mechanism and kinetics of the driving process [29,30]. Xie et al. showed that MEA can effectively cluster with sulfuric acid and significantly enhance new particle formation [23]. They showed that the removal rate of MEA due to this process was comparable to the rate of MEA oxidation by $\bullet\text{OH}$ at 217 K. Nevertheless, the complete role of MEA in environmental chemistry and aerosol chemistry remains unclear.

This study investigates the importance of direct SO_2 reactions in sulfate aerosol formation in the absence of $\bullet\text{OH}$ radicals. Long-term measurements have continually revealed the presence of abundant ammonia and amines in ambient air, including in the marine environment [31,32], and their role has mainly been limited to stabilizing sulfate clusters. Herein, we have investigated sulfate formation from SO_2 oxidation assisted by MEA using density functional theory calculations and kinetic modeling. The investigated SO_2 oxidation assisted by MEA is not only a potential source for atmospheric sulfate, but also a removal pathway for MEA. The kinetics of the studied reaction were evaluated and its implication in sulfate aerosol modeling was assessed.

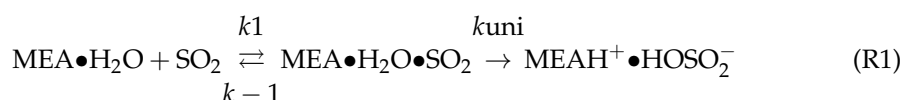
2. Methods

2.1. Quantum Chemical Calculations

Geometric optimizations of all stationary states of the studied reactions were conducted in Gaussian 09 using the ω B97X-D functional [33] in conjunction with the 6-311++G (3df,3pd) basis set. Vibrational frequency analysis and zero-point energies of ω B97XD/6-311++G (3df,3pd) structures were performed at the same level of theory under the harmonic oscillator-rigid rotor approximation at 298.15 K and 1 atm. This level of theory has been shown in previous studies to be sufficient for calculating the geometries and thermochemistry of atmospherically relevant systems [25,34–38]. Transition state configurations were determined using the synchronous transit quasi-Newton method [39] at the same level of theory, while single-point energy corrections on ω B97XD/6-311++G (3df,3pd) structures were performed at the DLPNO-CCSD(T)/aug-cc-pVTZ level of theory [40,41] using the ORCA 4.2.1 program package [42].

2.2. Reaction Kinetics Computation

The reaction rate constants were evaluated using the transition-state theory with the Wigner tunneling correction [43–45]. Previous studies have shown that the formation of a ternary complex from three separate reactants first proceeds through formation of a binary complex that interacts with the third species thereafter [46,47]. Given the high atmospheric concentration of water relative to those of other reactants, it is most likely that initial collisions between the three separate reactants (SO_2 , H_2O and MEA) will preferably form the hydrates of SO_2 and MEA prior to the formation of the ternary complex, $\text{MEA}\bullet\text{H}_2\text{O}\bullet\text{SO}_2$. Based on these considerations, $\text{SO}_2\bullet\text{H}_2\text{O}$ and $\text{MEA}\bullet\text{H}_2\text{O}$ will be determinant in computing the total rate constant of the MEA—assisted SO_2 hydrolysis. According to our calculations (see Table 1), $\text{MEA}\bullet\text{H}_2\text{O}$ is the most abundant binary complex among possible binary complexes and its interaction with SO_2 is likely to lead the process of MEA—mediated SO_2 hydrolysis according to the following equation:



Assuming equilibrium between $\text{MEA}\bullet\text{H}_2\text{O}\bullet\text{SO}_2$ and reactants $\text{MEA}\bullet\text{H}_2\text{O}$ and SO_2 based on the pseudo steady-state approximation, the overall rate of reaction (R1) can be written as:

$$v = k_{\text{MEA}\bullet\text{H}_2\text{O}\bullet\text{SO}_2} [\text{MEA}\bullet\text{H}_2\text{O}] [\text{SO}_2] \quad (1)$$

where $k_{\text{MEA}\bullet\text{H}_2\text{O}\bullet\text{SO}_2}$ is the reaction rate constant written as

$$k_{\text{MEA}\bullet\text{H}_2\text{O}\bullet\text{SO}_2} = \frac{k_1}{k_{-1}} k_{\text{uni}} = K_{\text{eq}} k_{\text{uni}} \quad (2)$$

k_1 is the collision frequency of $\text{MEA}\bullet\text{H}_2\text{O}$ and SO_2 to form $\text{MEA}\bullet\text{H}_2\text{O}\bullet\text{SO}_2$, k_{-1} is the decomposition rate constant of $\text{MEA}\bullet\text{H}_2\text{O}\bullet\text{SO}_2$ back to initial reactants, K_{eq} is the equilibrium constant of formation of the reactant complex, k_{uni} is the unimolecular rate constant of the reaction of the reactant complex to the product. The equilibrium constant is expressed as:

$$K_{\text{eq}} = \exp\left(-\frac{\Delta G_{\text{eq}}}{RT}\right) \quad (3)$$

where ΔG_{eq} is the Gibbs free energy change for the formation of the reactant complex, R is the gas constant, and T is the absolute temperature. k_{uni} is expressed as

$$k_{\text{uni}} = \Gamma \frac{k_{\text{B}}T}{h} \exp\left(-\frac{\Delta G^\ddagger}{RT}\right) \quad (4)$$

with ΔG^\ddagger being the activation Gibbs free energy change separating the reactant complex from the product state. Γ is the tunnelling effect factor, given by Wigner tunnelling correction:

$$\Gamma = 1 + \frac{1}{24} \left(\frac{h\nu^\ddagger}{k_B T} \right)^2 \quad (5)$$

where h is the Planck constant, ν^\ddagger the imaginary frequency of the transition state, k_B is the Boltzmann constant, T is the absolute temperature.

3. Results and Discussion

3.1. MEA—Assisted SO_2 Hydrolysis

As explained above, the formation of the ternary complex would proceed through the prior formation of the binary complex, followed by interaction with the third species [46,47]. According to our calculations, the formation of $\text{MEA}\bullet\text{H}_2\text{O}$ and $\text{H}_2\text{O}\bullet\text{SO}_2$ is more favorable than that of $\text{MEA}\bullet\text{H}_2\text{O}$ as can be seen from the equilibrium constants of their formation presented in Table 1. The two pathways of $\text{MEA}\bullet\text{H}_2\text{O}\bullet\text{SO}_2$ formation from $\text{MEA}\bullet\text{H}_2\text{O} + \text{SO}_2$ and $\text{H}_2\text{O}\bullet\text{SO}_2 + \text{MEA}$ interactions were readily assessed (see Figure 1). While the formation of $\text{MEA}\bullet\text{H}_2\text{O}$ is energetically more favorable (electronic energy change of $-5.49 \text{ kcal mol}^{-1}$ relative to precursor reactants) than $\text{H}_2\text{O}\bullet\text{SO}_2$ (electronic energy change of $-3.12 \text{ kcal mol}^{-1}$ relative to precursor reactants) due to higher ability to form hydrogen bonds, $\text{MEA}\bullet\text{H}_2\text{O}\bullet\text{SO}_2$ is formed from both $\text{MEA}\bullet\text{H}_2\text{O} + \text{SO}_2$ and $\text{H}_2\text{O}\bullet\text{SO}_2 + \text{MEA}$ interactions with nearly identical electronic energy changes, $-13.04 \text{ kcal mol}^{-1}$ and $-13.10 \text{ kcal mol}^{-1}$, respectively. The formation Gibbs free energies of these $\text{MEA}\bullet\text{H}_2\text{O}\bullet\text{SO}_2$ isomers at 298.15 K and 1 atm are similar within $1.70 \text{ kcal mol}^{-1}$, with the formation from $\text{MEA}\bullet\text{H}_2\text{O} + \text{SO}_2$ interaction being more favorable. Though both interactions will cumulatively form $\text{MEA}\bullet\text{H}_2\text{O}\bullet\text{SO}_2$ at standard atmospheric conditions, for simplicity, only the numerical results from $\text{MEA}\bullet\text{H}_2\text{O} + \text{SO}_2$ interaction are reported in Table 1.

Table 1. Electronic energy change (ΔE in kcal mol^{-1}) and Gibbs free energy change (ΔG in kcal mol^{-1}), equilibrium constants (K_{eq} , $\text{cm}^3 \text{ molecule}^{-1}$) of relevant reactions and equilibrium concentration (in molecule cm^{-3}) for some binary complexes in the MEA—assisted SO_2 hydrolysis, all calculated at 298.15 K and 1 atm. These electronic energy changes are plotted in Figures 1 and 3–6.

	ΔE	ΔG	K_{eq}	Concentration
$\text{MEA}\bullet\text{H}_2\text{O}$	−5.49	5.90	1.92×10^{-24}	3.63×10^9
$\text{SO}_2\bullet\text{H}_2\text{O}$	−3.12	4.94	9.85×10^{-24}	7.66×10^6
$\text{H}_2\text{O}\bullet\text{H}_2\text{O}$	−2.78	5.12	7.20×10^{-24}	4.35×10^{12}
$\text{MEA}\bullet\text{SO}_2$	−4.01	6.40	8.37×10^{-25}	2.03×10^3
$\text{MEA}\bullet\text{H}_2\text{O}\bullet\text{SO}_2$	−13.04	8.98		
TS1a	−6.21	16.86		
$\text{HOSO}_2^- \bullet \text{MEA}\text{H}^+$	−11.14	15.77		
$\text{O}_3\bullet\text{HOSO}_2^- \bullet \text{MEA}\text{H}^+$	−37.05	−3.61		
TS5	−16.99	−1.29		
$\text{HO}_2\bullet\text{OSO}_3^- \bullet \text{MEA}\text{H}^+$ (PD1)	−75.84	−5.85		
TS6	−67.21	−2.78		
$\text{HSO}_4^- \bullet \text{MEA}\text{H}^+ \bullet \text{O}_2$	−84.71	−0.76		
$\text{NO}_2\bullet\text{HOSO}_2^- \bullet \text{MEA}\text{H}^+$	−2.76	5.79		
TS3	22.82	37.96		
$\text{HSO}_4^- \bullet \text{MEA}\text{H}^+ \bullet \text{NO}$	−34.15	−3.42		
With an additional water molecule				

Table 1. Cont.

	ΔE	ΔG	K_{eq}	Concentration
MEA•H ₂ O•H ₂ O	−13.14	9.67		
MEA•2H ₂ O•SO ₂	−18.28	15.41		
TS2	−14.61	18.09		
HOSO ₂ [−] •MEA ⁺ •H ₂ O	−23.35	15.47		
O ₃ +HOSO ₂ [−] •MEA ⁺ +H ₂ O → HSO ₄ [−] •MEA ⁺ •O ₂ •H ₂ O	−93.89	−6.83		
NO ₂ •HOSO ₂ [−] •MEA ⁺ •H ₂ O	−15.74	5.43		
TS4a	30.35	51.96		
HSO ₄ [−] •MEA ⁺ •NO•H ₂ O	−46.46	−23.30		
TS4b	11.24	33.33		
SO ₃ [−] •MEA ⁺ •HONO•H ₂ O	−15.24	9.19		

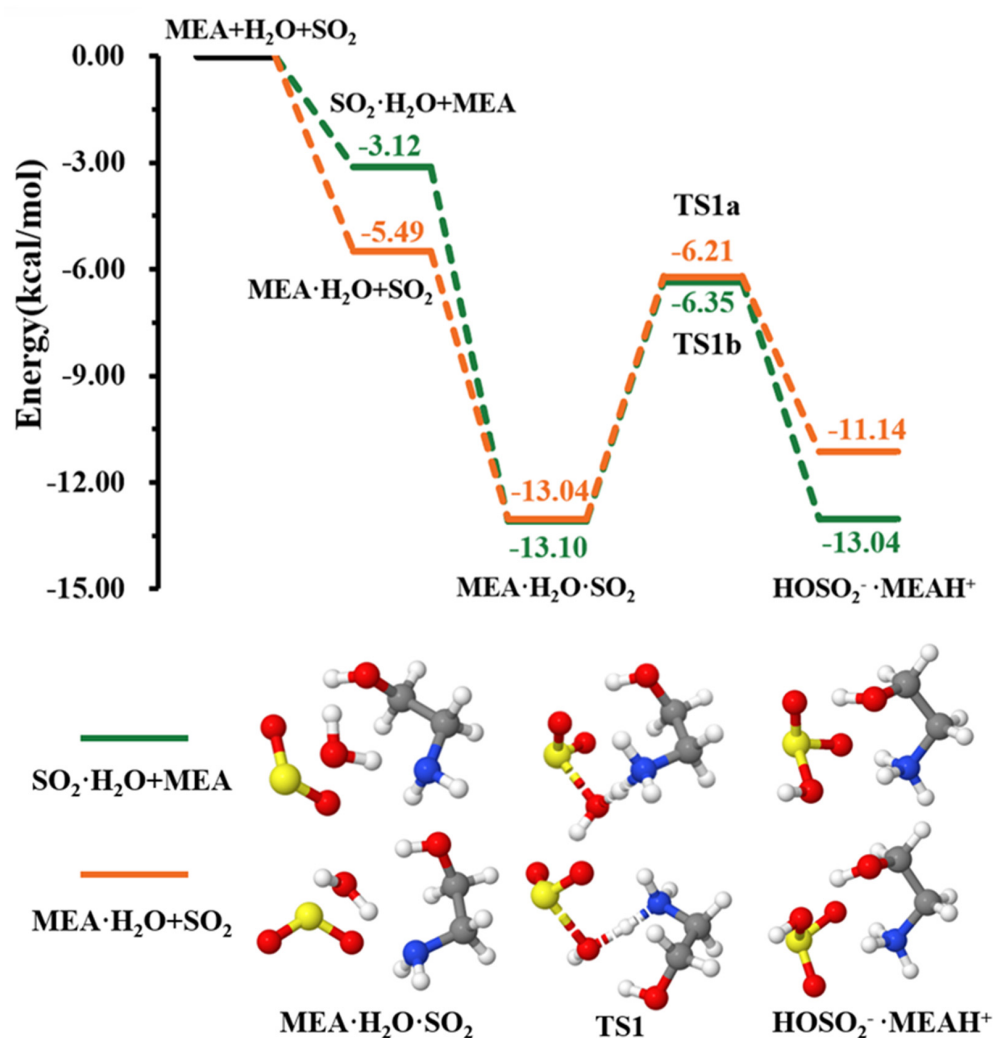


Figure 1. Energy surface for the MEA—catalyzed SO₂ hydrolysis. Color coding is yellow for sulfur atoms, red for oxygen atoms, white for hydrogen atoms, and blue for nitrogen atoms. Electronic energy values of all stationary states are indicated, and corresponding Gibbs-free energy values are presented in Table 1.

This complex rearranges through a transition state configuration located at -6.21 kcal mol $^{-1}$ below separate reactants, to form HOSO $_2^-$ •MEA H^+ . As expected from the average local ionization energy mapped van der Waals surface shown in Figure 2, the nitrogen atom is the reactive site of MEA in this process. This is the site with the most deficient potential, which is hence the most susceptible to undergo an electrophilic addition.

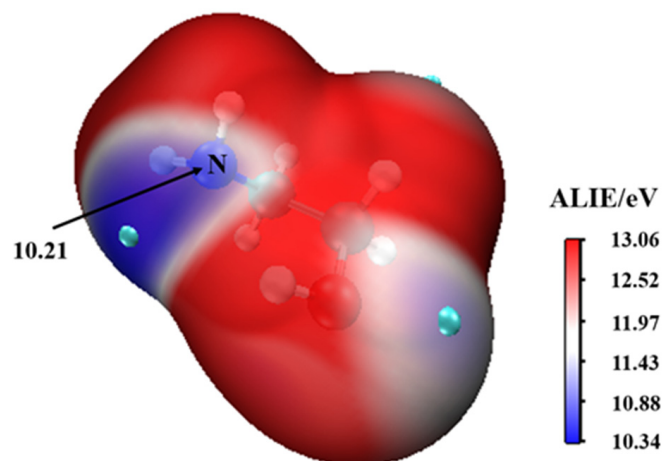


Figure 2. The average local ionization energy (ALIE/eV) of MEA.

The electronic energy barrier height in HOSO $_2^-$ •MEA H^+ formation is 6.83 kcal mol $^{-1}$, much lower than the 33.9 kcal mol $^{-1}$ energy barrier in the SO $_2$ + H $_2$ O → H $_2$ SO $_3$ reaction, as reported in a much earlier study [48]. A previous quantum chemical study showed that ammonia can lower the barrier height of SO $_2$ hydrolysis to \sim 12.0 kcal mol $^{-1}$ [49]; however, it is still higher than that reported for the MEA—assisted SO $_2$ hydrolysis in the current study. Much lower barriers were determined in SO $_2$ hydrolysis assisted by methylamine (5.80 kcal mol $^{-1}$) and dimethylamine (3.17 kcal mol $^{-1}$) [50]. Despite little differences that may arise as the result of different theoretical methods, the decreasing effect of ammonia, MEA, methylamine, and dimethylamine on the energy barrier in SO $_2$ hydrolysis is in line with the order of their basicity [51]. This further confirms the stronger ability of amines, compared to ammonia, to promote SO $_2$ hydrolysis.

Our calculations indicate that although a second water molecule did not explicitly participate in the reaction, it contributed to further reducing the energy barrier height for HOSO $_2^-$ •MEA H^+ formation down to 4.18 kcal mol $^{-1}$, rendering the SO $_2$ hydrolysis more favorable, as shown in the energy profile of Figure 3. Similar effects of water in decreasing energy barrier heights in chemical processes have been observed in several previous studies [49,52–54].

3.2. Further Reaction with NO $_2$

The sulfite ion in HOSO $_2^-$ •MEA H^+ is susceptible to react with relevant atmospheric oxidants. For example, it can be oxidized by NO $_2$ to form the HSO $_4^-$ (reaction (R4)). The different steps in this process are the formation of an intermediate complex, HOSO $_2^-$ •MEA H^+ •NO $_2$ lying at -2.76 kcal mol $^{-1}$, and overcoming a relatively high energy barrier prior to HSO $_4^-$ •MEA H^+ •NO formation (see Figure 4). The energy barrier in this process is 25.58 kcal mol $^{-1}$, which drastically increases to 46.09 kcal mol $^{-1}$ in the presence of an additional water molecule (reaction (R5), Figure 5). This substantial increase in the energy barrier height is the result of a strong stability of the reactant complex due to additional water that facilitates the formation of a tighter ring structure than without water. Even though this process is highly exergonic (with -23.42 kcal mol $^{-1}$ free energy change at 298.15 K and 1 atm), the high energy barrier would prevent this reaction at standard conditions. Moreover, the formation of nitrous oxide (HONO) in the HONO•SO $_3^-$ •MEA H^+ product

complex was observed to be a potential product in $\text{HOSO}_2^- \bullet \text{MEA}^+ \bullet \text{NO}_2$ decomposition in the presence of an additional water molecule (reaction (R6)).

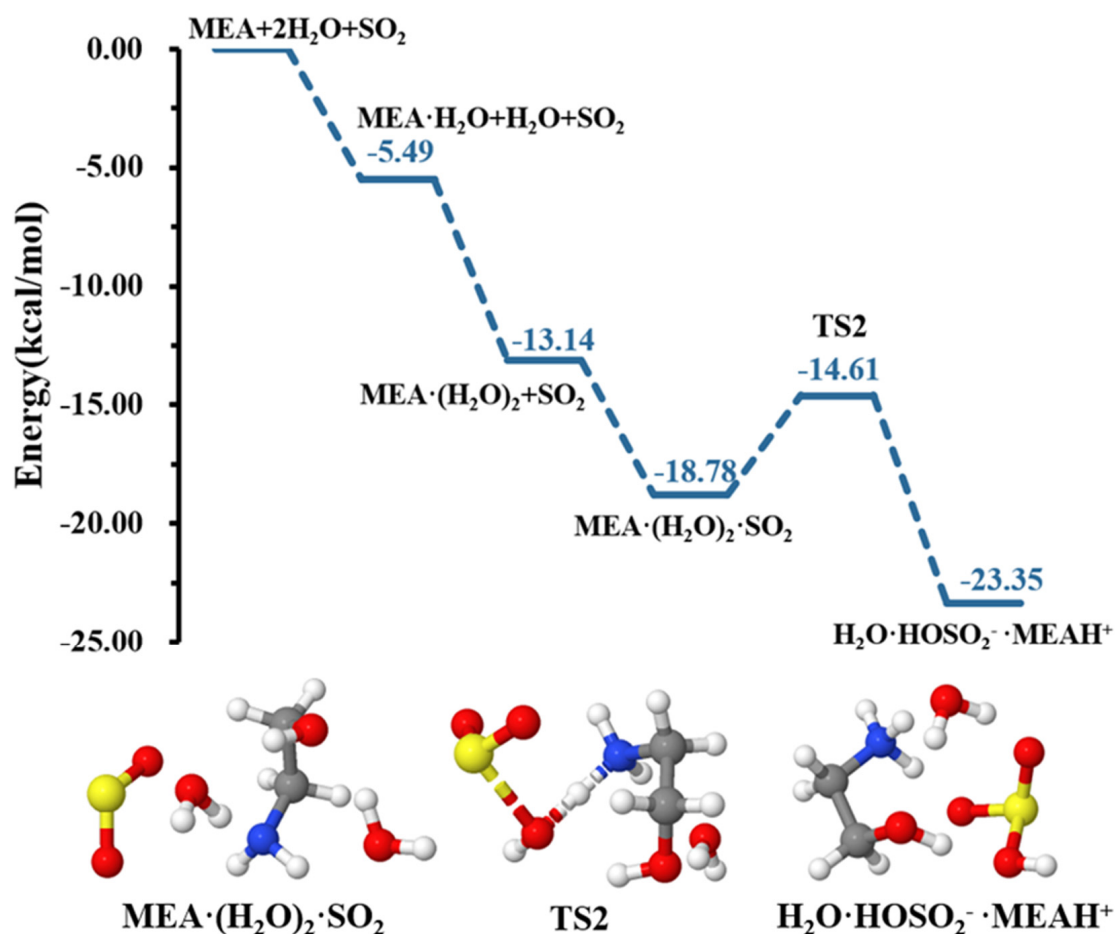


Figure 3. Energy surface for the MEA—catalyzed SO_2 hydrolysis with the presence of an additional water molecule. Color coding is yellow for sulfur atoms, red for oxygen atoms, white for hydrogen atoms, and blue for nitrogen atoms. Electronic energy values of all stationary states are indicated, and corresponding Gibbs-free energy values are presented in Table 1.

The energy barrier in this decomposition is $26.97 \text{ kcal mol}^{-1}$, being $19.11 \text{ kcal mol}^{-1}$ lower than the barrier in HSO_4^- formation. Despite the somewhat more favorable formation of HONO than HSO_4^- from $\text{HOSO}_2^- \bullet \text{MEA}^+$ oxidation by NO_2 in the presence of water, the overall rate of HONO formation would be limited given the relatively high energy barrier to its formation. A similar conclusion was observed by Wang et al. while studying the SO_2 hydrolysis assisted by methylamine and dimethylamine [50]. The fate of $\text{HOSO}_2^- \bullet \text{MEA}^+$ would then depends on other oxidants, such as O_3 .

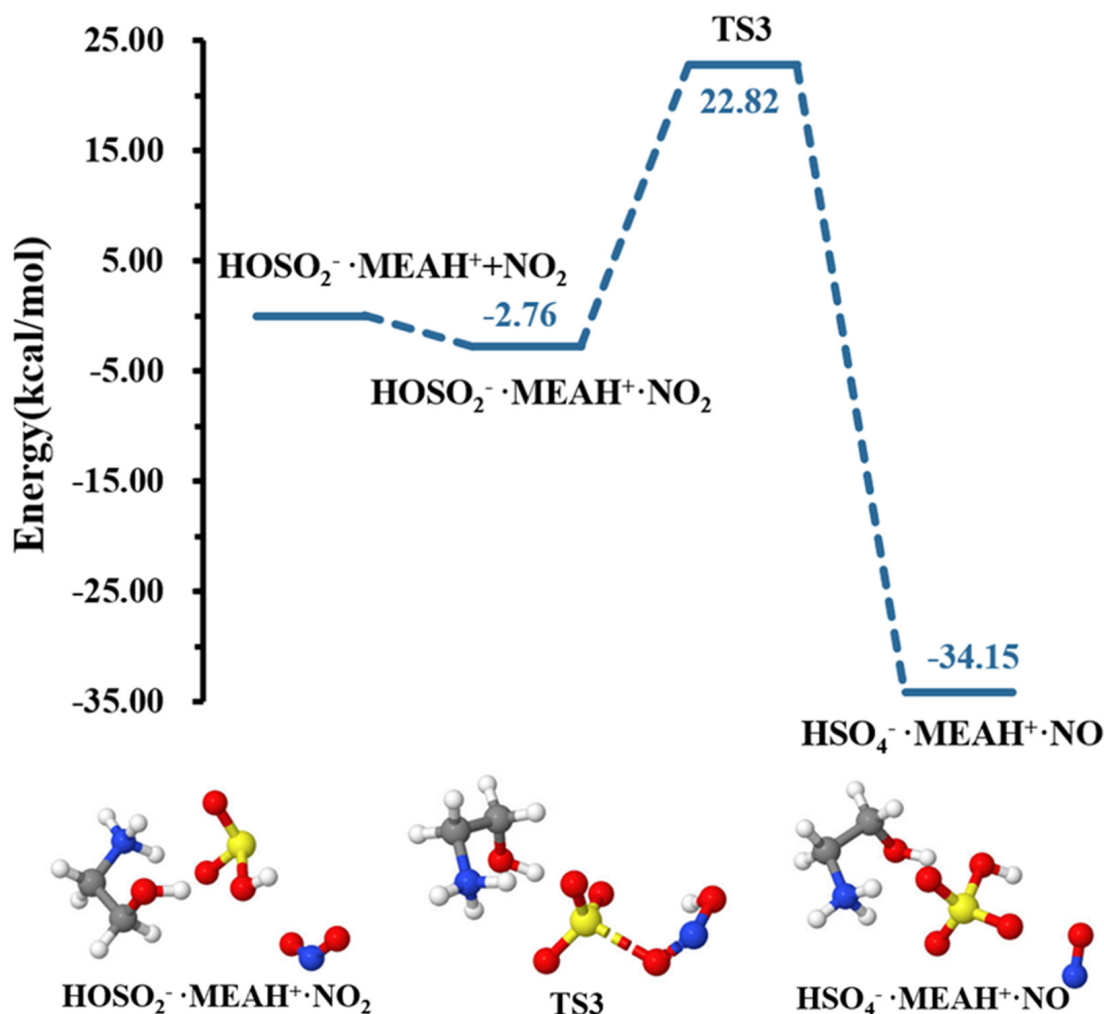


Figure 4. Potential energy profile for the oxidation reaction of HOSO₂•MEAH⁺ and NO₂. Color coding is yellow for sulfur atoms, red for oxygen atoms, white for hydrogen atoms, and blue for nitrogen atoms. Electronic energy values of all stationary states are indicated, and corresponding Gibbs-free energy values are presented in Table 1.

3.3. Further Reaction with O₃

The reaction of HOSO₂•MEAH⁺ with O₃ proceeds through the formation of the O₃•HOSO₂•MEAH⁺ intermediate complex (reaction (R7)). Thereafter, a double intramolecular transfer occurs within the complex: O transfer from O₃ to HOSO₂ to form HO₂–OSO₃•MEAH⁺ and H transfer from HO₂ fragment to OSO₃ fragment, resulting in the formation of O₂•HSO₄•MEAH⁺, as shown in Figure 6. These two processes were separated by energy barriers of 20.05 and 8.63 kcal mol⁻¹, respectively. Although the H transfer is relatively easy, i.e., characterized by a relatively low barrier, the O transfer constitutes the limiting step in O₂•HSO₄•MEAH⁺ formation. Compared to the reaction with NO₂, the conversion of HOSO₂•MEAH⁺ by reaction with O₃ is kinetically and thermodynamically more favorable, especially given the relatively low energy barrier and the substantial energy gain in the later process. It is well-known that molecular oxygen can adopt singlet and triplet spin configurations. Our attempts to compute the HOSO₂•MEAH⁺ reaction with O₃ on the triplet surface did not converge to O₂•HSO₄•MEAH⁺. Hence, the calculations in this process were performed on the singlet surface, exclusively. It is then obvious that although the O₂ molecule in O₂•HSO₄•MEAH⁺ would initially form in the singlet state, collision with other atmospheric species will quickly convert it to the triplet state, the most stable state of molecular oxygen in the atmosphere.

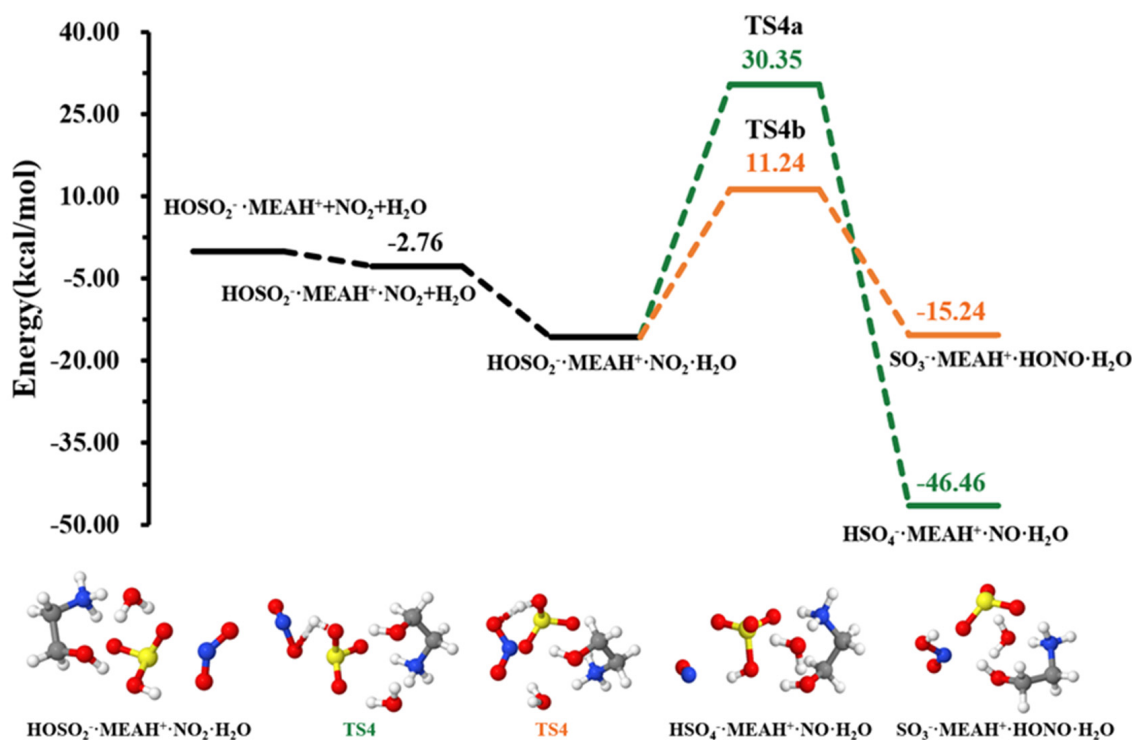


Figure 5. Potential energy profiles for the oxidation reaction for $\text{HOSO}_2^- \bullet \text{MEAH}^+$ and NO_2 , with additional H_2O . Color coding is yellow for sulfur atoms, red for oxygen atoms, white for hydrogen atoms, and blue for nitrogen atoms. Electronic energy values of all stationary states are indicated, and corresponding Gibbs-free energy values are presented in Table 1.

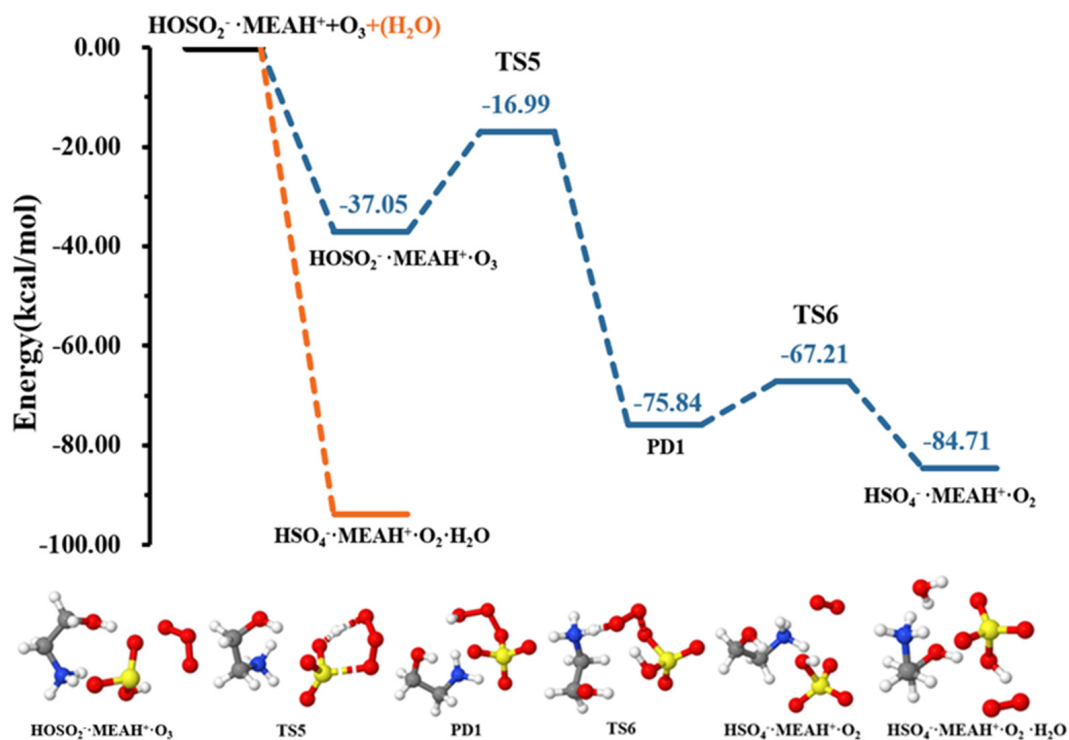


Figure 6. Potential energy profiles for the oxidation reaction for $\text{HOSO}_2^- \bullet \text{MEAH}^+$ and O_3 (with additional H_2O). Color coding is yellow for sulfur atoms, red for oxygen atoms, white for hydrogen atoms, and blue for nitrogen atoms. Electronic energy values of all stationary states are indicated, and corresponding Gibbs-free energy values are presented in Table 1.

Contrary to the effect of water in the $\text{HOSO}_2^- \bullet \text{MEA}^+ + \text{NO}_2$, the presence of additional water molecules significantly promotes the conversion of $\text{HOSO}_2^- \bullet \text{MEA}^+$ to $\text{HSO}_4^- \bullet \text{MEA}^+$ by reaction with O_3 , which becomes barrierless (see Figure 6). This effect of additional water is contrary to that observed in the reaction with NO_2 . The effect of water in promoting O_3^- oxidation reactions was also observed in our previous studies [52]. It is speculated that different reactive behaviors of MEA—assisted SO_2 hydrolysis towards NO_2 and O_3 compared to methylamine-assisted and dimethylamine-assisted SO_2 hydrolysis [51] can be attributed to the electronic effect of the $\bullet\text{OH}$ group in MEA.

3.4. Kinetics of MEA—Assisted SO_2 Hydrolysis and Implications for Atmospheric Sulfate Formation

As introduced in Section 2.2, the rate constant of MEA—assisted SO_2 hydrolysis is determined by considering the formation of the pre-reactive complex from $\text{MEA} \bullet \text{H}_2\text{O} + \text{SO}_2$ and $\text{SO}_2 \bullet \text{H}_2\text{O} + \text{MEA}$ interactions, given the high atmospheric concentration of water relative to those of other reactants. This is further justified by the values of equilibrium constants and equilibrium concentrations (presented in Table 1) of the three possible binary complexes susceptible to form from the interactions between MEA, SO_2 and H_2O . Assuming $[\text{SO}_2] \sim 10^{12}$ molecule cm^{-3} , $[\text{MEA}] \sim 2.43 \times 10^{15}$ molecule cm^{-3} and $[\text{H}_2\text{O}] \sim 7.77 \times 10^{17}$ molecule cm^{-3} corresponding to highly polluted conditions [29,55–57], $\text{MEA} \bullet \text{H}_2\text{O}$ has the highest equilibrium concentration among all the binary complexes. Hence, we determined the bimolecular rate constant of the MEA—assisted SO_2 hydrolysis based on the $\text{MEA} \bullet \text{H}_2\text{O} + \text{SO}_2$ interaction to be 1.90×10^{-14} cm^3 molecule $^{-1}$ s $^{-1}$ at 298.15 K. All reaction rate constants at this temperature are presented in Table 2, while the positive temperature-dependency of the rate constant is plotted in Figure 7. Taking into account the equilibrium concentration of $\text{MEA} \bullet \text{H}_2\text{O}$, which is equal to 3.63×10^9 cm^3 molecule $^{-1}$ as provided in Table 1, and the SO_2 concentration given above, we obtain a reaction rate (calculated according to Equation (1) of 6.89×10^7 molecule cm^{-3} s $^{-1}$ for the SO_2 hydrolysis assisted by MEA at 300 K. This rate is one order of magnitude higher than the estimated rate of SO_2 oxidation by $\bullet\text{OH}$ determined to be 1.50×10^6 molecule cm^{-3} s $^{-1}$ at the same temperature [57], considering an average $\bullet\text{OH}$ concentration of $\sim 10^6$ molecule cm^{-3} during daytime and 1.30×10^{-12} cm^3 molecule $^{-1}$ s $^{-1}$ rate constant of SO_2 oxidation by $\bullet\text{OH}$.

Table 2. Unimolecular (k_{uni} , s $^{-1}$) and bimolecular (k_{bimol} , cm^3 molecule $^{-1}$ s $^{-1}$) rate constants in the MEA—assisted SO_2 oxidation, all calculated at 298.15 K and 1 atm.

Reaction	k_{uni}	k_{bimol}
$\text{MEA} \bullet \text{H}_2\text{O} + \text{SO}_2 \rightarrow \text{HOSO}_2^- \bullet \text{MEA}^+$ (R2)	8.33×10^7	1.90×10^{-14}
$\text{MEA} \bullet (\text{H}_2\text{O})_2 + \text{SO}_2 \rightarrow \text{HOSO}_2^- \bullet \text{MEA}^+ \bullet \text{H}_2\text{O}$ (R3)	7.64×10^9	1.93×10^{-14}
$\text{NO}_2 + \text{HOSO}_2^- \bullet \text{MEA}^+ \rightarrow \text{HSO}_4^- \bullet \text{MEA}^+ \bullet \text{NO}$ (R4)	1.29×10^{-6}	
$\text{NO}_2 + \text{HOSO}_2^- \bullet \text{MEA}^+ + \text{H}_2\text{O} \rightarrow \text{HSO}_4^- \bullet \text{MEA}^+ \bullet \text{NO} \bullet \text{H}_2\text{O}$ (R5)	1.70×10^{-21}	
$\text{NO}_2 + \text{HOSO}_2^- \bullet \text{MEA}^+ + \text{H}_2\text{O} \rightarrow \text{SO}_3^- \bullet \text{MEA}^+ \bullet \text{HONO} \bullet \text{H}_2\text{O}$ (R6)	2.41×10^{-7}	
$\text{O}_3 + \text{HOSO}_2^- \bullet \text{MEA}^+ \rightarrow \text{HO}_2 \bullet \text{OSO}_3^- \bullet \text{MEA}^+$ (R7)	1.35×10^{-2}	
$\text{HO}_2 \bullet \text{OSO}_3^- \bullet \text{MEA}^+ \rightarrow \text{O}_2 \bullet \text{HSO}_4^- \bullet \text{MEA}^+$ (R8)	4.74×10^6	

Although the presence of additional water molecules increases the unimolecular rate constant of hydrated $\text{HOSO}_2^- \bullet \text{MEA}^+$ formation by two orders of magnitude relative to the reaction with one water molecule less, the overall effect on the bimolecular rate constant is reduced by the weaker binding between $\text{MEA} \bullet (\text{H}_2\text{O})_2$ and SO_2 to form the reactant complex, $\text{MEA} \bullet (\text{H}_2\text{O})_2 \bullet \text{SO}_2$. For this reaction, we obtain a rate constant of 1.93×10^{-14} cm^3 molecule $^{-1}$ s $^{-1}$ at 298.15 K. Similar to the reaction without additional water, the rate constant of the reaction in the presence of additional water exhibits a positive temperature-dependent variation in the range 200–400 K, though the effect is significantly

weak. Considering $[(\text{H}_2\text{O})_2] \sim 4.35 \times 10^{12} \text{ molecule cm}^{-3}$ according to our calculations, the reaction rate of SO_2 hydrolysis assisted by MEA with additional water was estimated to be $3.88 \times 10^3 \text{ molecule cm}^{-3} \text{ s}^{-1}$, three order of magnitude lower than the estimated rate of SO_2 oxidation by $\bullet\text{OH}$ reported previously [57].

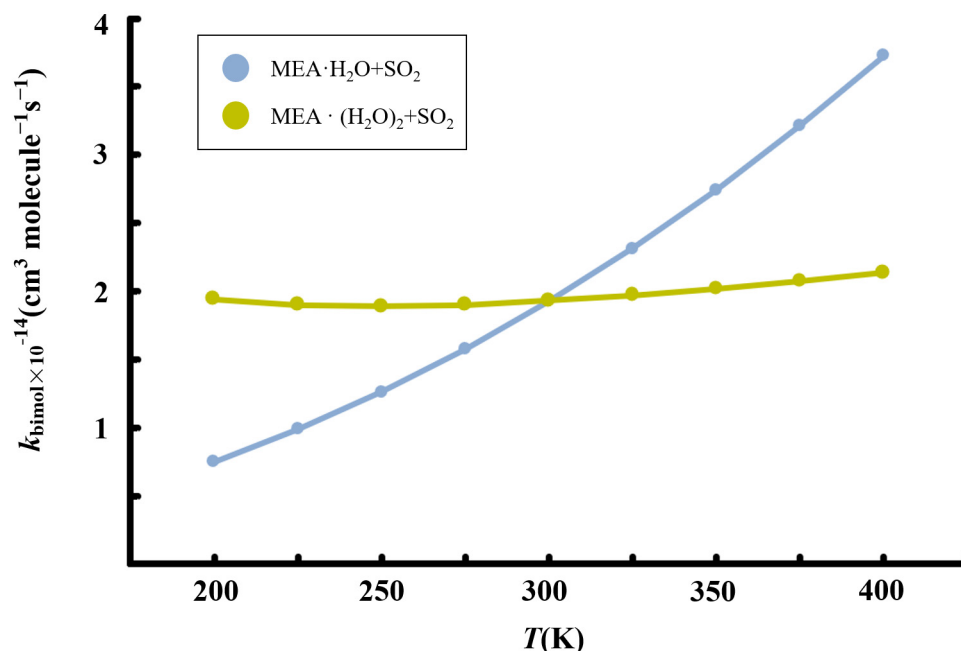


Figure 7. Calculated temperature-dependent rate constants for the MEA + $(\text{H}_2\text{O})_{1-2} + \text{SO}_2$ reaction at 1 atm.

Given the high rate of MEA—assisted SO_2 hydrolysis, it is evident that under extremely polluted conditions such as during haze events where there is insufficient $\bullet\text{OH}$ production due to low ultraviolet solar radiation, the investigated pathway might be a highly competitive process in atmospheric SO_2 oxidation.

Further exploration of the chemistry of $\text{HOSO}_2^- \bullet \text{MEA}^+$ shows that oxidation by NO_2 and O_3 to form $\text{HSO}_4^- \bullet \text{MEA}^+$ occurs with unimolecular rate constants of $1.29 \times 10^{-6} \text{ s}^{-1}$ and $1.35 \times 10^{-2} \text{ s}^{-1}$, respectively. With the presence of additional water molecules, $\text{HOSO}_2^- \bullet \text{MEA}^+$ decomposition by O_3 to form $\text{HSO}_4^- \bullet \text{MEA}^+$ is essentially barrierless, whereas decomposition by NO_2 is further prevented by a high energy barrier. For the reaction with NO_2 in the presence of water, instead, the decomposition of $\text{HOSO}_2^- \bullet \text{MEA}^+$ to $\text{HONO} \bullet \text{SO}_3^- \bullet \text{MEA}^+$ is slightly preferred. The relevance of $\text{HONO} \bullet \text{SO}_3^- \bullet \text{MEA}^+$ can be found both in $\bullet\text{OH}$ production through HONO and in sulfate formation through SO_3^- . $\text{HONO} \bullet \text{SO}_3^- \bullet \text{MEA}^+$ is formed at a unimolecular rate constant of $2.41 \times 10^{-7} \text{ s}^{-1}$; however, this is still much lower than the rate constant of the reaction with O_3 . This indicates that the reaction with O_3 is the most likely process for $\text{HOSO}_2^- \bullet \text{MEA}^+$ oxidation leading to sulfate formation in the gas phase.

Besides its fate in sulfate formation, the studied mechanism could also be an efficient removal pathway for MEA, which is believed to potentially represent an environmental risk [56,58]. So far, the reported sink processes for MEA include gas-phase oxidation by $\bullet\text{OH}$ and $\bullet\text{Cl}$, and reactive uptake by sulfuric acid molecules [22,59,60]. Rate constants of $7.10 \times 10^{-11} \text{ cm}^3 \text{ molecule}^{-1} \text{ s}^{-1}$ and $\sim 10^{-10} \text{ cm}^3 \text{ molecule}^{-1} \text{ s}^{-1}$ were reported for MEA oxidation by $\bullet\text{OH}$ and $\bullet\text{Cl}$, respectively [59,60]. With average $\bullet\text{OH}$ concentrations of $\sim 10^6 \text{ molecule cm}^{-3}$ during daytime and $\bullet\text{Cl}$ concentration of $\sim 10^5 \text{ molecule cm}^{-3}$, the estimated rates of MEA + $\bullet\text{OH}$ ($1.73 \times 10^{11} \text{ molecule cm}^{-3} \text{ s}^{-1}$) and MEA + $\bullet\text{Cl}$ ($2.43 \times 10^{10} \text{ molecule cm}^{-3} \text{ s}^{-1}$) are respectively 5×10^3 and 7×10^2 times higher than the rate of MEA + $\text{H}_2\text{O} + \text{SO}_2$ reaction. Under highly polluted conditions with elevated concen-

trations of MEA and low $\bullet\text{OH}$ concentration induced by low solar radiation, the mechanism reported in this study may also be a competitive pathway in MEA removal processes.

4. Conclusions

Sulfate formation was investigated from MEA—assisted SO_2 oxidation using first-principles simulations. Results indicate that decomposition of the direct SO_2 hydrolysis product, $\text{HOSO}_2^- \bullet\text{MEA}^+$, by O_3 is more favored than by NO_2 . The presence of additional water was found to play a varied role in the further oxidation process of $\text{HOSO}_2^- \bullet\text{MEA}^+$, significantly facilitating the decomposition by O_3 while substantially preventing the reaction with NO_2 . Besides sulfate formation mechanisms including ion-mediated and acid-catalyzed mechanisms that have already been elucidated in some previous studies, the current mechanism is an alternative pathway for sulfate formation and can be used to explain elevated sulfate formation observed under severe haze events where there is insufficient $\bullet\text{OH}$ production for SO_2 oxidation. Moreover, the presence of water introduces an additional feature, i.e., the HONO formation, in the reaction with NO_2 , though at a relatively lower rate. This latter mechanism might be a potential source for $\bullet\text{OH}$ under low ultraviolet solar radiation. We found that the title reaction can significantly outperform $\text{SO}_2 + \bullet\text{OH}$ reaction under low $\bullet\text{OH}$ conditions, providing new pathways for sulfate formation that would prevail under conditions of heavy pollution, high humidity, and low solar radiation, such as during haze events. The MEA—assisted SO_2 oxidation would also potentially compete with the $\bullet\text{OH}$ oxidation pathway in MEA removal processes under such conditions. This study highlights the role of alkanolamines in SO_2 oxidation, with implication in sulfate aerosol formation.

Author Contributions: Conceptualization, N.T.T.; methodology, N.T.T. and X.L.; formal analysis, X.L., N.T.T., S.N.T. and J.N.G.; investigation, X.L.; data curation, X.L. and N.T.T.; writing—original draft preparation, X.L.; writing—review and editing, M.L., S.N.T., J.N.G. and N.T.T.; supervision, L.D. and N.T.T.; funding acquisition, L.D. and N.T.T. All authors have read and agreed to the published version of the manuscript.

Funding: This research was funded by National Key Research and Development Program of China (2023YFC3706203), National Natural Science Foundation of China (22376121), and Natural Science Foundation of Shandong Province (ZR2023MD041).

Institutional Review Board Statement: Not applicable.

Informed Consent Statement: Not applicable.

Data Availability Statement: The data presented in this study are available on request from the corresponding authors. The data are not publicly available due to data sharing policy.

Acknowledgments: The authors acknowledge support from the Wuxi Hengding Supercomputing Center Co., Ltd.

Conflicts of Interest: The authors declare no conflicts of interests.

References

1. Hu, M.; Wu, Z.; Slanina, J.; Lin, P.; Liu, S.; Zeng, L. Acidic gases, ammonia and water-soluble ions in $\text{PM}_{2.5}$ at a coastal site in the Pearl River Delta, China. *Atmos. Environ.* **2008**, *42*, 6310–6320. [[CrossRef](#)]
2. Lai, S.C.; Zou, S.C.; Cao, J.J.; Lee, S.C.; Ho, K.F. Characterizing ionic species in $\text{PM}_{2.5}$ and PM_{10} in four pearl river delta cities, south china. *J. Environ. Sci.* **2007**, *19*, 939–947. [[CrossRef](#)] [[PubMed](#)]
3. Cheng, Y.; Zheng, G.; Wei, C.; Mu, Q.; Zheng, B.; Wang, Z.; Gao, M.; Zhang, Q.; He, K.; Carmichael, G.; et al. Reactive nitrogen chemistry in aerosol water as a source of sulfate during haze events in China. *Sci. Adv.* **2016**, *2*, e1601530. [[CrossRef](#)] [[PubMed](#)]
4. Cohen, A.J.; Brauer, M.; Burnett, R.; Anderson, H.R.; Frostad, J.; Estep, K.; Balakrishnan, K.; Brunekreef, B.; Dandona, L.; Dandona, R.; et al. Estimates and 25-year trends of the global burden of disease attributable to ambient air pollution: An analysis of data from the Global Burden of Diseases Study 2015. *Lancet* **2017**, *389*, 1907–1918. [[CrossRef](#)] [[PubMed](#)]
5. Liu, T.; Chan, A.W.H.; Abbatt, J.P.D. Multiphase oxidation of sulfur dioxide in aerosol particles: Implications for sulfate formation in polluted environments. *Environ. Sci. Technol.* **2021**, *55*, 4227–4242. [[CrossRef](#)] [[PubMed](#)]

6. Fan, M.; Zhang, Y.; Lin, Y.; Li, J.; Cheng, H.; An, N.; Sun, Y.; Qiu, Y.; Cao, F.; Fu, P. Roles of Sulfur Oxidation Pathways in the Variability in Stable Sulfur Isotopic Composition of Sulfate Aerosols at an Urban Site in Beijing, China. *Environ. Sci. Technol. Lett.* **2020**, *7*, 883–888. [[CrossRef](#)]
7. Zheng, B.; Zhang, Q.; Zhang, Y.; He, K.B.; Wang, K.; Zheng, G.J.; Duan, F.K.; Ma, Y.L.; Kimoto, T. Heterogeneous chemistry: A mechanism missing in current models to explain secondary inorganic aerosol formation during the January 2013 haze episode in North China. *Atmos. Chem. Phys.* **2015**, *15*, 2031–2049. [[CrossRef](#)]
8. Li, Y.; Han, Z.; Song, Y.; Li, J.; Sun, Y.; Wang, T. Impacts of the COVID-19 lockdown on atmospheric oxidizing capacity and secondary aerosol formation over the Beijing-Tianjin-Hebei region in Winter-Spring 2020. *Atmos. Environ.* **2023**, *295*, 119540. [[CrossRef](#)]
9. Wang, J.; Xing, J.; Wang, S.; Mathur, R.; Wang, J.; Zhang, Y.; Liu, C.; Pleim, J.; Ding, D.; Chang, X.; et al. The pathway of impacts of aerosol direct effects on secondary inorganic aerosol formation. *Atmos. Chem. Phys.* **2022**, *22*, 5147–5156. [[CrossRef](#)]
10. Zhang, X.; Zhang, K.; Liu, H.; Lv, W.; Aikawa, M.; Liu, B.; Wang, J. Pollution sources of atmospheric fine particles and secondary aerosol characteristics in Beijing. *J. Environ. Sci.* **2020**, *95*, 91–98. [[CrossRef](#)]
11. Shao, J.; Chen, Q.; Wang, Y.; Lu, X.; He, P.; Sun, Y.; Shah, V.; Martin, R.V.; Philip, S.; Song, S.; et al. Heterogeneous sulfate aerosol formation mechanisms during wintertime Chinese haze events: Air quality model assessment using observations of sulfate oxygen isotopes in Beijing. *Atmos. Chem. Phys.* **2019**, *19*, 6107–6123. [[CrossRef](#)]
12. Gen, M.; Zhang, R.; Huang, D.D.; Li, Y.; Chan, C.K. Heterogeneous SO₂ Oxidation in Sulfate Formation by Photolysis of Particulate Nitrate. *Environ. Sci. Technol. Lett.* **2019**, *6*, 86–91. [[CrossRef](#)]
13. Xue, J.; Yu, X.; Yuan, Z.; Griffith, S.M.; Lau, A.K.H.; Seinfeld, J.H.; Yu, J.Z. Efficient control of atmospheric sulfate production based on three formation regimes. *Nat. Geosci.* **2019**, *12*, 977–982. [[CrossRef](#)]
14. Itahashi, S.; Hattori, S.; Ito, A.; Sadanaga, Y.; Yoshida, N.; Matsuki, A. Role of Dust and Iron Solubility in Sulfate Formation during the Long-Range Transport in East Asia Evidenced by ¹⁷O-Excess Signatures. *Environ. Sci. Technol.* **2022**, *56*, 13634–13643. [[CrossRef](#)] [[PubMed](#)]
15. Alexander, B.; Allman, D.J.; Amos, H.M.; Fairlie, T.D.; Dachs, J.; Hegg, D.A.; Sletten, R.S. Isotopic constraints on the formation pathways of sulfate aerosol in the marine boundary layer of the subtropical northeast Atlantic Ocean. *J. Geophys. Res. Atmos.* **2012**, *117*, D06304. [[CrossRef](#)]
16. Chen, Q.; Sherwen, T.; Evans, M.; Alexander, B. DMS oxidation and sulfur aerosol formation in the marine troposphere: A focus on reactive halogen and multiphase chemistry. *Atmos. Chem. Phys.* **2018**, *18*, 13617–13637. [[CrossRef](#)]
17. Harris, E.; Sinha, B.; van Pinxteren, D.; Tilgner, A.; Fomba, K.W.; Schneider, J.; Roth, A.; Gnauk, T.; Fahlbusch, B.; Mertes, S.; et al. Enhanced role of transition metal ion catalysis during in-cloud oxidation of SO₂. *Science* **2013**, *340*, 727–730. [[CrossRef](#)]
18. Zhao, D.; Song, X.; Zhu, T.; Zhang, Z.; Liu, Y.; Shang, J. Multiphase oxidation of SO₂ by NO₂ on CaCO₃ particles. *Atmos. Chem. Phys.* **2018**, *18*, 2481–2493. [[CrossRef](#)]
19. Gao, J.; Shi, G.; Zhang, Z.; Wei, Y.; Tian, X.; Feng, Y.; Russell, A.G.; Nenes, A. Targeting Atmospheric Oxidants Can Better Reduce Sulfate Aerosol in China: H₂O₂ Aqueous Oxidation Pathway Dominates Sulfate Formation in Haze. *Environ. Sci. Technol.* **2022**, *56*, 10608–10618. [[CrossRef](#)]
20. Liu, T.; Clegg, S.L.; Abbatt, J.P.D. Fast oxidation of sulfur dioxide by hydrogen peroxide in deliquesced aerosol particles. *Proc. Natl. Acad. Sci. USA* **2020**, *117*, 1354–1359. [[CrossRef](#)]
21. Karl, M.; Wright, R.F.; Berglen, T.F.; Denby, B. Worst case scenario study to assess the environmental impact of amine emissions from a CO₂ capture plant. *Int. J. Greenh. Gas Control* **2011**, *5*, 439–447. [[CrossRef](#)]
22. Tian, X.; Chu, Y.; Chan, C.K. Reactive Uptake of Monoethanolamine by Sulfuric Acid Particles and Hygroscopicity of Monoethanolaminium Salts. *Environ. Sci. Technol. Lett.* **2022**, *9*, 16–21. [[CrossRef](#)]
23. Xie, H.; Elm, J.; Halonen, R.; Myllys, N.; Kurtén, T.; Kulmala, M.; Vehkamäki, H. Atmospheric Fate of Monoethanolamine: Enhancing New Particle Formation of Sulfuric Acid as an Important Removal Process. *Environ. Sci. Technol.* **2017**, *51*, 8422–8431. [[CrossRef](#)] [[PubMed](#)]
24. Liang, J.; Han, H.; Li, W.; Ma, X.; Xu, L. Experimental study on the absorption enhancement of CO₂ by MDEA-MEA based nanofluids. *Can. J. Chem. Eng.* **2022**, *100*, 3335–3344. [[CrossRef](#)]
25. Zhang, T.; Yu, Y.; Zhang, Z. Effects of non-aqueous solvents on CO₂ absorption in monoethanolamine: Ab initio calculations. *Mol. Simul.* **2018**, *44*, 815–825. [[CrossRef](#)]
26. Feron, P.; Conway, W.; Puxty, G.; Wardhaugh, L.; Green, P.; Maher, D.; Fernandes, D.; Cousins, A.; Shiwang, G.; Lianbo, L.; et al. Amine Based Post-Combustion Capture Technology Advancement for Application in Chinese Coal Fired Power Stations. *Energy Procedia* **2014**, *63*, 1399–1406. [[CrossRef](#)]
27. Reynolds, A.J.; Verheyen, T.V.; Adeloju, S.B.; Chaffee, A.L.; Meuleman, E. Primary sources and accumulation rates of inorganic anions and dissolved metals in a MEA absorbent during PCC at a brown coal-fired power station. *Int. J. Greenh. Gas Control* **2015**, *41*, 239–248. [[CrossRef](#)]
28. Veltman, K.; Singh, B.; Hertwich, E.G. Human and Environmental Impact Assessment of Postcombustion CO₂ Capture Focusing on Emissions from Amine-Based Scrubbing Solvents to Air. *Environ. Sci. Technol.* **2010**, *44*, 1496–1502. [[CrossRef](#)]
29. Miller, D.D.; Chuang, S.S.C. Experimental and Theoretical Investigation of SO₂ Adsorption over the 1,3-Phenylenediamine/SiO₂ System. *J. Phys. Chem. C* **2015**, *119*, 6713–6727. [[CrossRef](#)]

30. You, Y.; Kanawade, V.P.; de Gouw, J.A.; Guenther, A.B.; Madronich, S.; Sierra-Hernández, M.R.; Lawler, M.; Smith, J.N.; Takahama, S.; Ruggeri, G.; et al. Atmospheric amines and ammonia measured with a chemical ionization mass spectrometer (CIMS). *Atmos. Chem. Phys.* **2014**, *14*, 12181–12194. [[CrossRef](#)]
31. Gao, Y.; Chen, D.; Shen, Y.; Gao, Y.; Gao, H.; Yao, X. Mapping gaseous dimethylamine, trimethylamine, ammonia, and their particulate counterparts in marine atmospheres of China's marginal seas—Part 2: Spatiotemporal heterogeneity, causes, and hypothesis. *Atmos. Chem. Phys.* **2022**, *22*, 1515–1528. [[CrossRef](#)]
32. Zhong, Q.E.; Cheng, C.; Wang, Z.; Li, L.; Li, M.; Ge, D.; Wang, L.; Li, Y.; Nie, W.; Chi, X.; et al. Diverse mixing states of amine-containing single particles in Nanjing, China. *Atmos. Chem. Phys.* **2021**, *21*, 17953–17967. [[CrossRef](#)]
33. Chai, J.; Head-Gordon, M. Long-range corrected hybrid density functionals with damped atom–atom dispersion corrections. *Phys. Chem. Chem. Phys.* **2008**, *10*, 6615–6620. [[CrossRef](#)] [[PubMed](#)]
34. Elm, J.; Jen, C.N.; Kurtén, T.; Vehkamäki, H. Strong Hydrogen Bonded Molecular Interactions between Atmospheric Diamines and Sulfuric Acid. *J. Phys. Chem. A* **2016**, *120*, 3693–3700. [[CrossRef](#)] [[PubMed](#)]
35. Elm, J.; Myllys, N.; Hyttinen, N.; Kurtén, T. Computational Study of the Clustering of a Cyclohexene Autoxidation Product C₆H₈O₇ with Itself and Sulfuric Acid. *J. Phys. Chem. A* **2015**, *119*, 8414–8421. [[CrossRef](#)]
36. Elm, J.; Myllys, N.; Luy, J.; Kurtén, T.; Vehkamäki, H. The effect of water and bases on the clustering of a cyclohexene autoxidation product C₆H₈O₇ with sulfuric acid. *J. Phys. Chem. A* **2016**, *120*, 2240–2249. [[CrossRef](#)]
37. Li, H.; Zhong, J.; Vehkamäki, H.; Kurtén, T.; Wang, W.; Ge, M.; Zhang, S.; Li, Z.; Zhang, X.; Francisco, J.S.; et al. Self-Catalytic Reaction of SO₃ and NH₃ To Produce Sulfamic Acid and Its Implication to Atmospheric Particle Formation. *J. Am. Chem. Soc.* **2018**, *140*, 11020–11028. [[CrossRef](#)]
38. Myllys, N.; Olenius, T.; Kurtén, T.; Vehkamäki, H.; Riipinen, I.; Elm, J. Effect of Bisulfate, Ammonia, and Ammonium on the Clustering of Organic Acids and Sulfuric Acid. *J. Phys. Chem. A* **2017**, *121*, 4812–4824. [[CrossRef](#)]
39. Peng, C.; Ayala, P.Y.; Schlegel, H.B.; Frisch, M.J. Using redundant internal coordinates to optimize equilibrium geometries and transition states. *J. Comput. Chem.* **1996**, *17*, 49–56. [[CrossRef](#)]
40. Riplinger, C.; Neese, F. An efficient and near linear scaling pair natural orbital based local coupled cluster method. *J. Chem. Phys.* **2013**, *138*, 034106. [[CrossRef](#)]
41. Riplinger, C.; Sandhoefer, B.; Hansen, A.; Neese, F. Natural triple excitations in local coupled cluster calculations with pair natural orbitals. *J. Chem. Phys.* **2013**, *139*, 134101. [[CrossRef](#)] [[PubMed](#)]
42. Neese, F. The ORCA program system. *Wires. Comput. Mol. Sci.* **2012**, *2*, 73–78. [[CrossRef](#)]
43. Duchovic, R.J.; Pettigrew, J.D.; Welling, B.; Shipchandler, T. Conventional transition state theory/Rice–Ramsperger–Kassel–Marcus theory calculations of thermal termolecular rate coefficients for H(D)+O₂+M. *J. Chem. Phys.* **1996**, *105*, 10367–10379. [[CrossRef](#)]
44. Elm, J.; Jørgensen, S.; Bilde, M.; Mikkelsen, K.V. Ambient reaction kinetics of atmospheric oxygenated organics with the OH radical: A computational methodology study. *Phys. Chem. Chem. Phys.* **2013**, *15*, 9636–9645. [[CrossRef](#)] [[PubMed](#)]
45. Wu, R.; Pan, S.; Li, Y.; Wang, L. Atmospheric oxidation mechanism of toluene. *J. Phys. Chem. A* **2014**, *118*, 4533–4547. [[CrossRef](#)] [[PubMed](#)]
46. Buszek, R.J.; Barker, J.R.; Francisco, J.S. Water Effect on the OH + HCl Reaction. *J. Phys. Chem. A* **2012**, *116*, 4712–4719. [[CrossRef](#)]
47. Wine, P.H.; Thompson, R.J.; Ravishankara, A.R.; Semmes, D.H.; Gump, C.A.; Torabi, A.; Nicovich, J.M. Kinetics of the Reaction OH + SO₂ + M → HOSO₂ + M. Temperature and Pressure Dependence in the Falloff Region. *J. Chem. Phys.* **1984**, *88*, 2095–2104. [[CrossRef](#)]
48. Liu, J.; Fang, S.; Liu, W.; Wang, M.; Tao, F.; Liu, J. Mechanism of the Gaseous Hydrolysis Reaction of SO₂: Effects of NH₃ versus H₂O. *J. Phys. Chem. A* **2015**, *119*, 102–111. [[CrossRef](#)]
49. Buszek, R.J.; Torrent-Sucarrat, M.; Anglada, J.M.; Francisco, J.S. Effects of a Single Water Molecule on the OH + H₂O₂ Reaction. *Phys. Chem. A* **2012**, *116*, 5821–5829. [[CrossRef](#)]
50. Wang, S.; Zeng, X.C.; Li, H.; Francisco, J.S. A possible unaccounted source of atmospheric sulfate formation: Amine-promoted hydrolysis and non-radical oxidation of sulfur dioxide. *Chem. Sci.* **2020**, *11*, 2093–2102. [[CrossRef](#)]
51. Hall, H.K., Jr. Correlation of base strengths of amines. *J. Am. Chem. Soc.* **1957**, *79*, 5441–5444. [[CrossRef](#)]
52. Franchin, A.; Ehrhart, S.; Leppä, J.; Nieminen, T.; Gagné, S.; Schobesberger, S.; Wimmer, D.; Duplissy, J.; Riccobono, F.; Dunne, E.M.; et al. Experimental investigation of ion–ion recombination under atmospheric conditions. *Atmos. Chem. Phys.* **2015**, *15*, 7203–7216. [[CrossRef](#)]
53. Jara-Toro, R.A.; Hernandez, F.J.; Garavagno, M.; Taccone, R.A.; Pino, G.A. Water catalysis of the reaction between hydroxyl radicals and linear saturated alcohols (ethanol and n-propanol) at 294 K. *Phys. Chem. Chem. Phys.* **2018**, *20*, 27885–27896. [[CrossRef](#)] [[PubMed](#)]
54. Xu, L.; Tsona, N.T.; Tang, S.; Li, J.; Du, L. Role of (H₂O)_n (n = 1–2) in the Gas-Phase Reaction of Ethanol with Hydroxyl Radical: Mechanism, Kinetics, and Products. *ACS Omega* **2019**, *4*, 5805–5817. [[CrossRef](#)] [[PubMed](#)]
55. Rao, A.B.; Rubin, E.S. A Technical, Economic, and Environmental Assessment of Amine-Based CO₂ Capture Technology for Power Plant Greenhouse Gas Control. *Environ. Sci. Technol.* **2002**, *36*, 4467–4475. [[CrossRef](#)]
56. Sharma, S.D.; Azzi, M. A critical review of existing strategies for emission control in the monoethanolamine-based carbon capture process and some recommendations for improved strategies. *Fuel* **2014**, *121*, 178–188. [[CrossRef](#)]
57. Long, B.; Bao, J.L.; Truhlar, D.G. Reaction of SO₂ with OH in the atmosphere. *Phys. Chem. Chem. Phys.* **2017**, *19*, 8091–8100. [[CrossRef](#)]

58. Nielsen, C.J.; Herrmann, H.; Weller, C. Atmospheric chemistry and environmental impact of the use of amines in carbon capture and storage (CCS). *Chem. Soc. Rev.* **2012**, *41*, 6684–6704. [[CrossRef](#)]
59. Borduas, N.; Abbatt, J.P.D.; Murphy, J.G. Gas Phase Oxidation of Monoethanolamine (MEA) with OH Radical and Ozone: Kinetics, Products, and Particles. *Environ. Sci. Technol.* **2013**, *47*, 6377–6383. [[CrossRef](#)]
60. Xie, H.; Ma, F.; Wang, Y.; He, N.; Yu, Q.; Chen, J. Quantum Chemical Study on ·Cl-Initiated Atmospheric Degradation of Monoethanolamine. *Environ. Sci. Technol.* **2015**, *49*, 13246–13255. [[CrossRef](#)]

Disclaimer/Publisher’s Note: The statements, opinions and data contained in all publications are solely those of the individual author(s) and contributor(s) and not of MDPI and/or the editor(s). MDPI and/or the editor(s) disclaim responsibility for any injury to people or property resulting from any ideas, methods, instructions or products referred to in the content.